Resolving Material-Specific Structures within $Fe_3O_4|\gamma$-Mn_2O_3 Core|Shell Nanoparticles Using Anomalous Small-Angle X-ray Scattering (ASAXS)

K. L. Krycka,[*,†] J. A. Borchers,[†] G. Salazar-Alvarez,[‡] A. López-Ortega,[¶] M. Estrader,[‡] S. Estradé,[§] J. Sort,[⊥] F. Peiró,[∥] M. D. Baró,[#] C. C. Kao,[@] and J. Nogués[△]

NIST Center for Neutron Research, National Institute of Standards and Technology, Gaithersburg, Maryland 20899, Department of Materials and Environmental Chemistry, Stockholm University, S-10691 Stockholm, Sweden., CIN2 (ICN-CSIC) and Universitat Autònoma de Barcelona, Catalan Institute of Nanotechnology, Campus de la UAB, E-08193 Bellaterra (Barcelona), Spain., TEM-MAT, CCiT, Universitat de Barcelona, Solè i Sabarí s 1, E-08028 Barcelona, Spain., LENS, MIND-IN2UB, Department d'Electrònica, Universitat de Barcelona, Martí i Franquès 1, E-08028 Barcelona, Spain, Institució Catalana de Recerca i Estudis Avançats (ICREA) and Department de Física, Universitat Autònoma de Barcelona, E-08193 Bellaterra, Spain., Department de Física, Universitat Autònoma de Barcelona, E-08193 Bellaterra, Spain., Stanford Synchrotron Radiation Lightsource, Menlo Park, CA 94025, and Institució Catalana de Recerca i Estudis Avançats (ICREA) and CIN2 (ICN-CSIC) and Universitat Autònoma de Barcelona, Catalan Institute of Nanotechnology (ICN), Campus de la UAB, E-08193 Bellaterra (Barcelona), Spain.

E-mail: kathryn.krycka@nist.gov

Abstract

The material specific structure of monodispersed $Fe_3O_4|\gamma$-Mn_2O_3 core|shell nanoparticles is determined using multiple energy, anomalous, small-angle x-ray scattering (ASAXS). The contribution of each component to the total scattering profile is identified with unprecedented clarity. We show that $Fe_3O_4|\gamma$-Mn_2O_3 core|shell nanoparticles with a diameter of 8.2 nm $\pm$ 0.2 nm consist of a core with a composition near Fe_3O_4 surrounded by a $(Fe_{1-X}Mn_X)_3O_4$ shell with a graded composition, *i.e.*, ranging from X $\approx$ 0.40 at the inner shell toward X $\approx$ 0.46 at the surface. Evaluation of the scattering contribution arising from the interference between material-specific layers additionally reveals the presence of Fe_3O_4 cores without a coating shell. Importantly, the present analysis enhances the sensitivity of the method with regard to the chemical boundaries and internal nanoparticle morphology compared with traditional approaches. Finally, it is found that the material-specific scattering profile shapes and chemical compositions extracted by this method are independent of the original input chemical compositions used in the analysis, revealing multi-energy ASAXS as a powerful tool for determining internal nanostructured morphology even if the exact composition of the individual layers is not known *a priori*.

Introduction

The exceptional impact of nanoparticles in industry and research during the last decade is undeniable, spreading in fields with everyday applications such as cosmetics to high-end biotechnol-

*To whom correspondence should be addressed

†NIST Center for Neutron Research, National Institute of Standards and Technology, Gaithersburg, Maryland 20899

‡Department of Materials and Environmental Chemistry, Stockholm University, S-10691 Stockholm, Sweden.

¶CIN2 (ICN-CSIC) and Universitat Autònoma de Barcelona, Catalan Institute of Nanotechnology, Campus de la UAB, E-08193 Bellaterra (Barcelona), Spain.

§TEM-MAT, CCiT, Universitat de Barcelona, Solè i Sabarí s 1, E-08028 Barcelona, Spain.

‖LENS, MIND-IN2UB, Department d'Electrònica, Universitat de Barcelona, Martí i Franquès 1, E-08028 Barcelona, Spain

⊥Institució Catalana de Recerca i Estudis Avançats (ICREA) and Department de Física, Universitat Autònoma de Barcelona, E-08193 Bellaterra, Spain.

#Department de Física, Universitat Autònoma de Barcelona, E-08193 Bellaterra, Spain.

@Stanford Synchrotron Radiation Lightsource, Menlo Park, CA 94025

△Institució Catalana de Recerca i Estudis Avançats (ICREA) and CIN2 (ICN-CSIC) and Universitat Autònoma de Barcelona, Catalan Institute of Nanotechnology (ICN), Campus de la UAB, E-08193 Bellaterra (Barcelona), Spain.

ogy.[1–5] Interestingly, advances in synthetic chemistry have allowed reaching beyond conventional nanoparticles into more complex hybrid structures comprised of two (or more) materials such as core|shell particles.[6–8] These systems can combine in a synergetic way the diverse properties (*e.g.*, catalytical, optical, magnetic or biomedical) of the different constituents leading to multifunctional materials with novel and improved characteristics, paving the way for an even broader applicability of nanoparticles. Given the unprecedented ability to control growth parameters during the synthesis (*i.e.*, core diameter, shell thickness, and material composition) the overall properties of the particles can be accurately tailored to match specific applications. In fact, core|shell nanoparticles have an extra degree of freedom since the properties can often be tuned not only by the core and shell characteristics, but also through their interactions.[9–18] Typically, the properties of core|shell nanoparticles depend critically on the structural morphology such as the thickness (and variability) of the constituent layers, their composition, and the sharpness of interfaces. Consequently, the precise determination of these parameters is vital to understanding and fine tuning the functionalities of the core|shell systems.

While many techniques exist for non location-specific chemical analysis, such as Mössbauer spectroscopy[19,20] and x-ray absorption spectroscopy (XAS), characterizing the internal structure of such core|shell nanoparticles continues to be a challenging endeavor. Even high-resolution transmission electron microscopy (HR-TEM) imaging with electron energy loss spectroscopy (EELS) analysis,[21–27] which can often give an accurate account of the morphology of the particles, remains impractical since only a small number of particles can be analyzed. For this reason, neutron and x-ray diffractive methods are desirable since they measure macroscopic amounts of sample (*i.e.*, millions of nanoparticles), giving a better picture of the overall morphology and dispersion. Yet, small angle x-ray scattering (SAXS), which is very useful in evaluating particle size and polydispersity for homogeneous nanoparticles,[28,29] suffers from an inability to definitively pinpoint chemical boundaries within core|shell nanoparticles, even in cases for which high material contrast exists. To this end, the multiple-energy, anomalous SAXS (ASAXS) approach[30–33] offers renewed potential for the analysis of core|shell nanoparticles.[34,35] Here we demonstrate the full

utility of the ASAXS technique to unambiguously elucidate the fine structural details for a tightly-packed powder of 8.2 nm $\pm$ 0.2 nm diameter core|shell nanoparticles nominally comprised of Fe_3O_4 cores and γ-Mn_2O_3 shells.[36] The resonant x-ray results indicate the presence not only of a clear core|shell structure, but also the existence of an intermediate shell of mixed composition, in agreement with TEM and EELS analysis. Moreover, the study directly reveals differences in the degree of coating, which are largely undetectable by any other techniques.

Neutron and X-Ray Scattering

SAXS and small angle neutron scattering, SANS, provide structural information on the micron to sub-nanometer length scale (Fig. 1a). The measured intensity, I, which is plotted as a function of scattering wavevector, Q, in Fig. 1b for SANS and Fig. 1c for SAXS, is proportional to the material-specific scattering length density squared, $|\rho|^2$. For all variables $'$ and $''$ denote the real (scattering) and imaginary (absorbing) components. Information regarding the spatial distribution of the J scattering centers, located at the relative positions, R_J, is contained within the Fourier transform, $\mathfrak{F}$ as

$$I(Q) \propto \left| \sum_{\text{J scatterers}} (\rho'_J + i\rho''_J) e^{i\vec{Q}\cdot\vec{R}_J} \right|^2 = \left| \sum_{\text{K materials}} \rho_K \mathfrak{F}_K \right|^2 . \quad (1)$$

From a modeling standpoint, $|\mathfrak{F}|^2$ is viewed as the convolution of the structure factor (nanoparticle packing), $|S|^2$, with the form factor (internal nanoparticle structure), $|F|^2$.

Although diffraction methods can be extremely sensitive to external nanoparticle diameter, they are relatively insensitive to internal strucutres. As the room temperature SANS data underscore, even a high ρ contrast ratio > 4 (refer to Table I) is not sufficient to distinguish through modeling[37] whether the nanoparticles' $|F|^2$ is closer to homogeneous Fe-Mn-oxide spheres or arises from distinctive $Fe_3O_4|\gamma$-Mn_2O_3 core|shell nanoparticles. For example, as can be seen in Fig. 1b, the simulated patterns for homogeneous 8.2 nm $(Fe_{0.5}Mn_{0.5})_3O_4$ nanoparticles (red curve) and 7.2 nm core | 0.3 nm thick shell of $Fe_3O_4|\gamma$-Mn_2O_3 nanoparticles (green curve) are virtually indistinguishable. Both models employ a hard-sphere packing structure ($|S|^2$)[37] of radius 4.0 nm

and volume fraction of 0.45 to reproduce the lowest-Q oscillation. The polydispersity,[37] or full-width half maximum of the Gaussian distribution of nanoparticle diameters divided by the average nanoparticle radius, was gauged at ≈ 0.10 (*i.e.* a standard distribution of $\pm$ 0.82 nm for an average diameter of 8.2 nm). While hybrid models between these extremes of homogeneous sphere and distinct core|shell may be constructed that more closely resemble the data, it would be difficult to argue for the uniqueness of model.

Importantly, material sensitivity (and, thus, sensitivity to internal layering) may be enhanced by collecting multiple, energy-dependent scattering patterns of varied ρ's. For neutrons this can be achieved in many organic systems through hydrogen-deuterium substitution,[38,39] while for x-rays ρ changes dramatically as a function of energy about atomic absorption edges, coined anomalous or resonant scattering.[40] Thus, as shown in Fig. 1c, anomalous scattering patterns were acquired at the Mn and Fe K-edges,[41] 6535 eV and 7112 eV, respectively, and off-resonance at 6000 eV (Table I). Yet, aside from changes in total intensity and a slight low-Q oscillation shift, the profiles appear to be strikingly similar. The reason for this is that the scattering is heavily influenced by scattering interference between the Fe and Mn oxides (also referred as a cross term, which will be explicitly evaluated later on). To illustrate this, consider a two-layer system labeled as α and β, (α =Fe_3O_4 and $\beta = \gamma$-Mn_2O_3)

$$I(Q) \propto \underbrace{|\rho_\alpha|^2|\mathfrak{F}_\alpha|^2}_{I_\alpha} + \underbrace{|\rho_\beta|^2|\mathfrak{F}_\beta|^2}_{I_\beta} + \underbrace{2(\rho'_\alpha\rho'_\beta + \rho''_\alpha\rho''_\beta)\overbrace{(\mathfrak{F}'_\alpha\mathfrak{F}'_\beta + \mathfrak{F}''_\alpha\mathfrak{F}''_\beta)}^{\mathfrak{F}_{Int1}}}_{I_{Int1}} + \underbrace{2(\rho'_\alpha\rho''_\beta - \rho''_\alpha\rho'_\beta)\overbrace{(\mathfrak{F}''_\alpha\mathfrak{F}'_\beta - \mathfrak{F}'_\alpha\mathfrak{F}''_\beta)}^{\mathfrak{F}_{Int2}}}_{I_{Int2}}, \tag{2}$$

where cross terms, I_{Int1} and I_{Int2}, each depend on both ρ_α and ρ_β. It is clear that material-specific scattering cannot simply be extracted from the subtraction of scattering profiles obtained at energies just below and on a relevant absorption edge, as is commonly assumed.

However, the *simultaneous analysis* of multi-energy ASAXS profiles[34,35] does provide the means to uniquely separate material-specific $|\mathfrak{F}|^2$s. The number of input scattering scans with different energies must be equivalent to the total number of material-specific scattering terms and interference terms of interest. First, we note that I_{Int2} of Eq. 2 is negligibly small (Table I) and

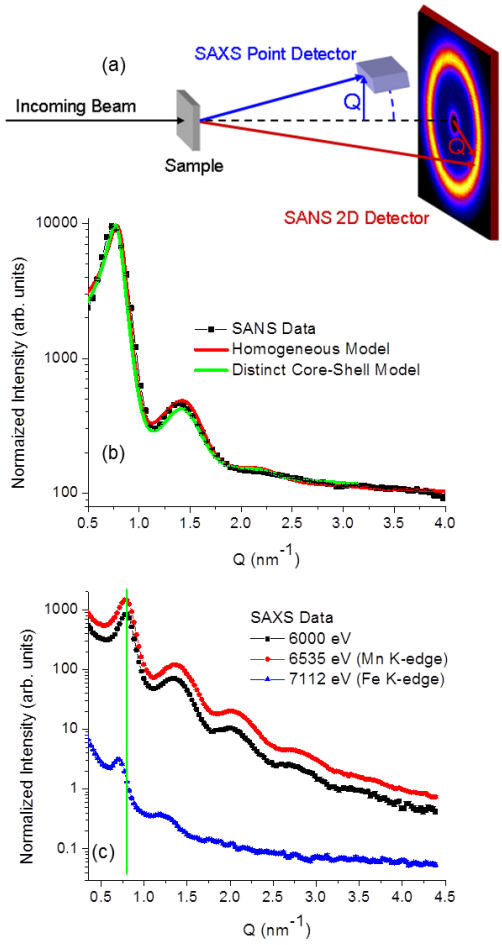

Figure 1: (a) Schematic of SAXS and SANS set-ups (not drawn to scale). Note that the experiments are carried out separately in different user facilities. (b) SANS data fitted using models based on homogeneous Fe-Mn-oxide nanoparticles (red curve) or distinct Fe_3O_4 core and γ-Mn_2O_3 shell structure (green curve). (c) SAXS data taken away from resonance (6000 eV) and on the Mn and Fe K-edges (6535 eV and 7112 eV, respectively). The vertical green line emphasizes low-Q oscillation shift observed at the Fe K-edge. The statistical counting error bars for SANS and SAXS data are included, but are too small to be seen.

Table 1: Scattering length densities (SLD $\rho = \rho' + i\rho''$, given in 10^{-4} nm^{-2}) for various crystallographic phases at different energies.[41] The SLD were calculated using mass densities of 4.90, 5.18, 4.50, and 4.86 $\frac{g}{cm^3}$ for γ-Fe_2O_3, Fe_3O_4, γ-Mn_2O_3, Mn_3O_4, respectively.
[a] X-ray
[b] Neutrons

	Phase	6000 eV[a]	6535 eV[a]	7112 eV[a]	λ_n = 0.5 nm[b]
ρ'	γ-Fe_2O_3	40.62	39.95	29.90	7.17
	Fe_3O_4	40.00	39.32	29.05	6.95
	γ-Mn_2O_3	33.74	25.03	34.30	1.71
	Mn_3O_4	48.65	35.59	49.50	1.54
ρ''	γ-Fe_2O_3	0.8259	0.7083	4.561	–
	Fe_3O_4	0.8328	0.7144	2.536	–
	γ-Mn_2O_3	0.6279	2.184	3.380	–
	Mn_3O_4	0.9267	3.263	5.059	–

can be disregarded. Thus, the remaining scattering terms can be uniquely isolated using only three scattering inputs taken at three different energies, E_1 - E_3, (Fig. 1c). At each point in Q-space, the material-specific scattering contributions are determined by inverting the following matrix:

$$\underbrace{\begin{bmatrix} |\rho_\alpha(E_1)|^2 & |\rho_\beta(E_1)|^2 & 2(\rho'_\alpha(E_1)\rho'_\beta(E_1)+\rho''_\alpha(E_1)\rho''_\beta(E_1)) \\ |\rho_\alpha(E_2)|^2 & |\rho_\beta(E_2)|^2 & 2(\rho'_\alpha(E_2)\rho'_\beta(E_2)+\rho''_\alpha(E_2)\rho''_\beta(E_2)) \\ |\rho_\alpha(E_3)|^2 & |\rho_\beta(E_3)|^2 & 2(\rho'_\alpha(E_3)\rho'_\beta(E_3)+\rho''_\alpha(E_3)\rho''_\beta(E_3)) \end{bmatrix}}_{Known\ Coefficients} \underbrace{\begin{bmatrix} |\mathfrak{F}\alpha|^2 \\ |\mathfrak{F}\beta|^2 \\ \mathfrak{F}_{Int1} \end{bmatrix}}_{Variables\ To\ Solve} \propto \underbrace{\begin{bmatrix} I(E_1) \\ I(E_2) \\ I(E_3) \end{bmatrix}}_{Numerical\ Inputs} \quad (3)$$

Application of Eq. 3 to the data of Fig. 1c results in the separation of Fe_3O_4 and γ-Mn_2O_3 material-specific scattering ($|\mathfrak{F}\alpha|^2$ and $|\mathfrak{F}\beta|^2$) plus the γ-Mn_2O_3-Fe_3O_4 cross term ($\mathfrak{F}_{Int1}$), as plotted in Fig. 2a. It is worth noting this separation approach yields scattering profiles that are directly correlated of the number of chemical formula units per volume squared rather than the traditional scattering length density squared which varies as a function of incident x-ray energy. Considering that the cross term contributes twice as much as $|\mathfrak{F}\alpha|^2$ or $|\mathfrak{F}\beta|^2$ (Eq. 2) to the overall scattering intensity, this explains the the similarity in scattering shape at all energies as shown in Fig. 1c. Although the interference term can be positively or negatively valued, simulation suggests that for core|shell morphology the cross term will contribute negatively over the first oscillation, as

experimentally observed. Moreover, the existence of a non-zero cross-term implies that there must be a correlation between the Fe_3O_4 and γ-Mn_2O_3 layers, *i.e.* a significant proportion of them must co-exist within the same nanoparticles with a repeating morphology particle-to-particle.

The difference in the material-specific scattering profiles is especially striking at 1.1 nm^{-1} where the γ-Mn_2O_3 scattering contains a noticeably sharper dip than the Fe_3O_4 scattering (Fig. 2b). Above Q = 1.5 nm^{-1} the profiles look similar. Extensive simulation suggests that if the relative intensity of each energy-dependent experimental profile is not preserved to within a few percent, then the extracted material-specific profiles will typically assume a common scattering shape similar to that of the composite nanoparticle. Thus, the low-intensity region of $Q \geq 1.5$ nm^{-1} is especially susceptible to any background subtraction issues during the material-specific scattering reconstruction. Even so there are periodic differences, indicated by green arrows (Fig. 2b). Division of the extracted Fe_3O_4 profile by the γ-Mn_2O_3 profile, $|\mathfrak{F}|_{Fe_3O_4}/|\mathfrak{F}|_{\gamma-Mn_2O_3}$, further highlights these periodic differences (Fig. 2c). These differences indicate that the Fe_3O_4 and γ-Mn_2O_3 components must be present in different morphological distributions as a function of radius within the nanoparticles, which for spherical nanoparticles would correspond to a radially graded (*i.e.* core|shell or core|shell|shell) structure.

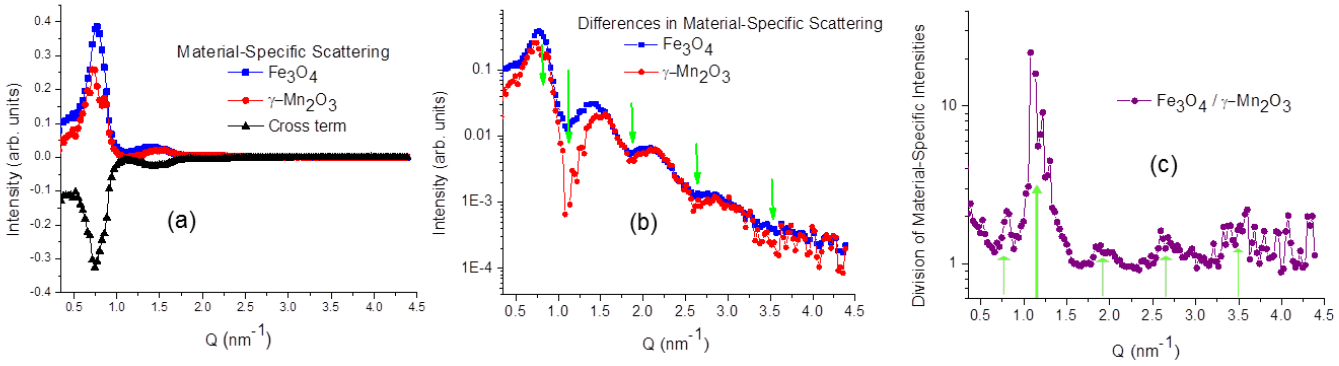

Figure 2: (a) Extracted, material-specific scattering profiles and cross term. (b) Arrows pinpoint the periodic differences between Fe_3O_4 and γ-Mn_2O_3. (c) Division of the material-specific profiles, $|\mathfrak{F}_{Fe_3O_4}|^2/|\mathfrak{F}_{\gamma-Mn_2O_3}|^2$, highlight the variation between Fe_3O_4 and γ-Mn_2O_3 scattering and indicate a difference in their nanoparticle morphologies.

Core-Shell Morphology

Modeling of the material-specific x-ray scattering provides ensemble-average information regarding nanoparticle core and shell dimensions, compositional uniformity, size polydispersity, nanoparticle packing, and the relative ratio of Mn to Fe present. As discussed previously in regard to modeling of the SANS data, $|\mathfrak{F}|^2 = |F|^2|S|^2$, where $|F|^2$ and $|S|^2$ are the form and structure factors, respectively.

Outermost Diameter: The γ-Mn_2O_3 (Fig. 2a-b) distribution extends out to the edge of the nanoparticle with scattering that is consistent with spherical model of exterior diameter 8.2 nm $\pm$ 0.1 nm. The corresponding interior can vary from a sphere of uniform density to a sphere centrally devoid of Mn up to the first 1.8 nm in diameter. (Even element-specific diffraction is most sensitive to the outermost dimensions of that layer since more material resides there.) In contrast, the Fe_3O_4 oscillations and slope (Fig. 2b) cannot be fit by a sphere of uniform density. Instead a graded model where the amount of Fe_3O_4 decreases radially towards the surface is required. Depending on the steepness of gradient chosen, the outer diameter can range from 8.2 nm (less gradient) to 8.4 nm (more gradient). However, since we know that the Fe_3O_4 should be concentrated toward the interior of the core|shell particles based on knowledge about their chemical synthesis,[36] we impose the constraint that the Fe_3O_4 outer diameter should not exceed that of the γ-Mn_2O_3. This constrains the average particle diameter to be 8.2 nm $\pm$ 0.2 nm.

Bimodal Distribution: The sharp γ-Mn_2O_3 dip at Q = 1.1 nm^{-1} (Fig. 2b) is indicative of very low polydispersity,[37] on the order of 2%. In light of the monodispersity of the γ-Mn_2O_3 shells, the associated Fe_3O_4 portion of the core|shell particles should also be monodisperse, yet the observed scattering (Fig. 2b) does not display such sharp features. To reconcile this, a bimodal model comprised of two different types of nanoparticles containing Fe_3O_4 is necessary. The model consists of (i) monodisperse Fe_3O_4 core with reduced Fe-density shell nanoparticles (whose outer shell diameter primarily dictates the dip locations observed) which are correlated with the γ-Mn_2O_3 shells, and (ii) uncoated seeds (whose contributions smooth out the dips) which are uncorrelated with the γ-Mn_2O_3 shells. This simple model can explain the diffusive Fe_3O_4 features without resorting to

an unphysically large polydispersity for the Fe_3O_4 distribution. The reciprocal space (Q) region surveyed was optimized for larger particles and, thus, it does not cover a full oscillatory pattern of the seeds necessary for a rigorous determination of their sizes. The modeled seed diameters ranged from $\approx$ 2.2 nm to 3.4 nm. The best Fe-based structure factor fit encompassing both the Fe_3O_4 component of the core|shell nanoparticles and of the Fe_3O_4 uncoated seeds consists of a hard sphere radius[37] of 4.2 nm and volume fraction of 0.44. The γ-Mn_2O_3 hard sphere structure factor, diverges slightly from this at volume fraction of 0.50 and hard-sphere radius of 4.0 nm required to capture the higher-Q shift of the first peak (Fig. 2a-b).

Layer Densities: Given these experimental constraints, the representative model (Fig. 3a and 3b) consists of a core|shell|shell nanoparticle of variable density. The inner core diameter is set at 0.8 nm $\pm$ 0.2 nm (to accommodate polydispersity), the inner shell thickness is 2 nm, and the remaining outer shell thickness is 1.7 nm (adding up to a total diameter of 8.2 nm $\pm$ 0.2 nm). Since we do not observe large changes in the relative densities of Fe_3O_4 and γ-Mn_2O_3 between the inner and outer shells, we feel this level of shell delineation provides sufficient grading without over determining the system. However, it should be noted that the choice of interior shell radii are somewhat arbitrary and other shell radii choices yield similar results. Within this model the Fe_3O_4 density (number of formula units per volume multiplied by a scalar) is best fit from the interior to exterior regions with values of 5.31 $\frac{units}{volume}$, 2.65 $\frac{units}{volume}$, and 2.32 $\frac{units}{volume}$, respectively (Fig. 3b). The γ-Mn_2O_3 component of our core|shell|shell model returns densities (also in formula units per volume that are consistently scaled with and directly comparable to the Fe_3O_4 densities) of 0 $\frac{units}{volume}$, 2.70 $\frac{units}{volume}$, and 3.00 $\frac{units}{volume}$ from interior to exterior, respectively (Fig. 3a). The γ-Mn_2O_3 fit is fairly insensitive to the core region given its relatively smaller contribution to the total scattering pattern than in the Fe_3O_4 case. Yet, it is reasonable to expect that the combined γ-Mn_2O_3 plus Fe_3O_4 density should not vary significantly throughout the particle and, thus, the sum should be close to 5.3 $\frac{units}{volume}$ for all layers. The Fe_3O_4 core region fit value of 5.31 $\frac{units}{volume}$ hence drives the resulting γ-Mn_2O_3 density toward zero, though we cannot completely exclude the possibility that some Mn might reside within the core region. It is worthwhile to note that the division of the

γ-Mn_2O_3 and Fe_3O_4 models (Fig. 3c) reproduces all the primary experimental features observed in Fig. 2b-c and strongly reinforces the core|graded-shell model.

Seed Fraction Estimate: As modeled, the uncoated Fe_3O_4 seeds can vary between 2.2 nm to 3.4 nm in diameter. When these seeds are modeled with pure Fe_3O_4 spheres of diameter 2.2 nm and polydispersity of 30% (Fig. 3b) their scattering profile must be scaled by a factor of 0.15 compared with the core|shell particles, indicating that the number of uncoated seeds are $\approx$ 15% that of the core|shell particles. If we employ a larger seed model closer of 3.4 nm in diameter this seed:core|shell ratio drops as the seed volume squared (*i.e.* $\approx$ 4%).

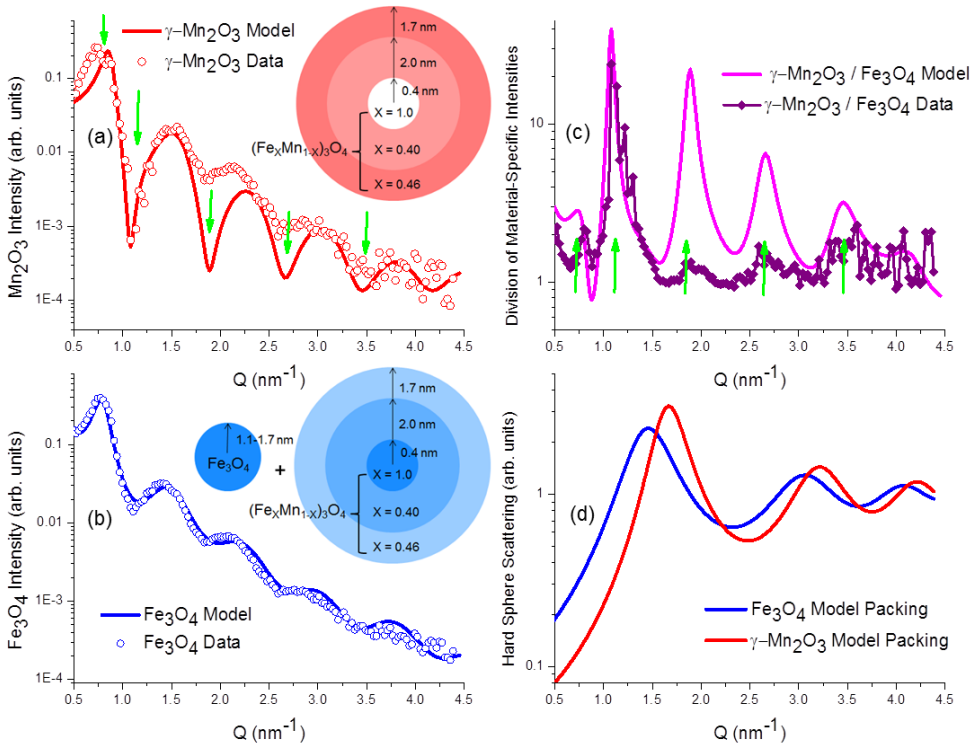

Figure 3: (a) γ-Mn_2O_3 scattering profile and fit where dips highlighted with arrows correspond to those of Fig. 2a. (b) Fe_3O_4 scattering profile and fit. Although the insets in (a) and (b) which depict the γ-Mn_2O_3 and Fe_3O_4 portions of the model are not drawn to scale, their fit dimensions are listed exactly as modeled. (c) Division of Fe_3O_4 and γ-Mn_2O_3 modeled scattering profiles reproduces the experimental features of Fig. 2c. (d) Hard-sphere model $|S|^2$s of core|shell nanoparticles and uncoated seed nanoparticles.

Nanoparticle Packing

Structure Factor Variation: The difference in modeled packing structure $|S|^2$ for the γ-Mn_2O_3 and Fe_3O_4 scattering contributions, depicted in Fig. 3d, can arise only if a portion of the Mn and Fe atoms are not all contained within the same set of nanoparticles, consistent with Fe_3O_4-only seeds. (Note that this is by ne means inconsistent with the presence of a cross term, Fig 2a, which arises from Mn and Fe atoms contained within the set of nanoparticles and can be attributed to the distinctly different core-shell nanoparticles.) The shift to slightly larger average spacing between particles and a slightly lower packing density (embodied by $|S|^2$ of the Fe_3O_4 compared with γ-Mn_2O_3) is also consistent with the presence of randomly dispersed, uncoated Fe_3O_4 seeds. Moreover, the experimentally-observed shift of the lowest-Q peak in the raw ASAXS scattering to a lower-Q value at the Fe K-edge (Fig. 1c) would be unexplained in the absence of a bimodal distribution. Although it may seem counter-intuitive that the peak should shift toward lower Q with decreased Fe scattering contribution at 7112 eV when the Fe_3O_4 $|S|^2$ peaks at lower Q than the γ-Mn_2O_3 $|S|^2$ (Fig. 3d), we note that the large, negatively-valued cross term (whose peak placement is determined by both the γ-Mn_2O_3 and the Fe_3O_4) also diminishes at the the Fe K-edge.

Cross Term: As a self-consistency check, we note that the third solved term from Eq. 3, $\mathfrak{F}_{Int1}$, *i.e.*, the cross term term, contains additional information about the material-specific $|S|^2$s. Division of the extracted terms, $|\mathfrak{F}_{Int1}|^2$ and $|\mathfrak{F}_{\alpha,\beta}|^2$, yields

$$\mathfrak{F}_{Int1}/(|\mathfrak{F}_{\alpha,\beta}|^2) = |F_{\beta,\alpha}|^2(S'^2_\alpha S'^2_\beta + S''^2_\alpha S''^2_\beta + 2S'_\alpha S'_\beta S''_\alpha S''_\alpha)/|S_{\alpha,\beta}|^2 \tag{4}$$

where F for a spherically symmetric object is always real. If $S_\alpha = S_\beta$ ($S_{Fe_3O_4} = S_{\gamma-Mn_2O_3}$), we should be able to re-extract $|\ddot{\mathfrak{F}}_{Fe_3O_4}|^2$ and $|\ddot{\mathfrak{F}}_{\gamma-Mn_2O_3}|^2$ using

$$\mathfrak{F}_{Int1}/(|\mathfrak{F}_{\alpha,\beta}|^2) = |S_{\beta,\alpha}|^2|F_{\beta,\alpha}|^2 = |\ddot{\mathfrak{F}}_{\beta,\alpha}|^2 \tag{5}$$

where the double dot in $|\ddot{\mathfrak{F}}_{\alpha,\beta}|$ indicates that the previously extracted $\mathfrak{F}_{Int1}$ and $|\mathfrak{F}_{\alpha,\beta}|^2$ (Eq. 2,3)

were utilized in this second-order reconstruction. The result of this procedure is shown in Fig. 4a. Although features similar to Fig. 2a are reproduced, the reconstruction using Eq. 4 differs noticeably in the circled region (specifically where the derived $|S_{Fe_3O_4}|^2$ and $|S_{\gamma-Mn_2O_3}|^2$ most strongly diverge in Fig. 3d). This deviance confirms that $S_{Fe_3O_4}$ and $S_{\gamma-Mn_2O_3}$, though similar, are not identical. The result is again in full agreement with our differing $|S|^2$ fits (Fig. 3d) and the experimental, first oscillation shift to lower-Q at the Fe K-edge (Fig. 1c), and it reinforces the model consisting of core|graded-shell nanoparticles residing alongside uncoated Fe_3O_4 seeds.

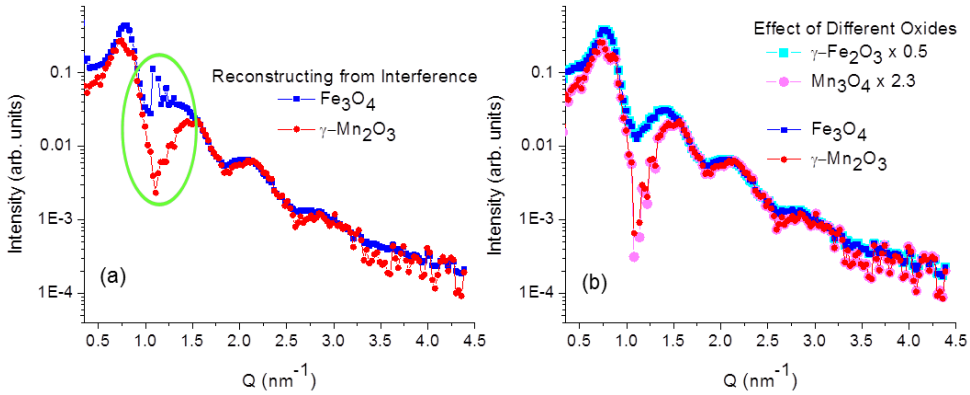

Figure 4: (a) Material-specific scattering reconstruction obtained using Eq. 4. (b) The effect oxide-variation in material-specific profile reconstruction using Eq. 3.

Compositional Analysis

Mn to Fe Ratio: The combined γ-Mn_2O_3 and Fe_3O_4 core|graded-shell fits produces a composite nanoparticle tending toward Fe_3O_4 in the center surrounded by a graded shell comprised of both Fe and Mn oxide. Using the fits described above the net chemical compositions are 5.31 $\frac{Fe_3O_4}{volume}$ | 2.65 $\frac{Fe_3O_4}{volume}$ + 2.70 $\frac{\gamma-Mn_2O_3}{volume}$ | 2.32 $\frac{Fe_3O_4}{volume}$ + 3.00 $\frac{\gamma-Mn_2O_3}{volume}$. If we were to assume that the shells are homogeneously mixed, then we can re-write the compositions in terms of Mn-ferrite as $(Mn_XFe_{1-X})_3O_{4.2}$, where X ranges from 0.40 to 0.46 for the average inner and outer shell regions, respectively. Since the ASAXS technique is optimized to be highly sensitive to the Fe and Mn content, yet less sensitive to the oxygen content, it is likely that the oxygen stoichiometric number

is in fact closer to 4.0.

Chemical Sensitivity: To determine the sensitivity of this technique to oxide type, we substitute the ρ's (Table I) of γ-Fe_2O_3 and Mn_3O_4 for Fe_3O_4 and γ-Mn_2O_3, respectively, into Eq. 3. As shown in Fig. 4b, the basic scattering shapes remain unaltered, while the difference between Fe and Mn oxide scattering profiles changes by a relative factor of 4.6. Taking into account the scaling of Fe-oxide core|shell and Mn-oxide shell scattering contributions with the fact that the measured intensity is proportional to density *squared*, we extract a mixed-shell composition of 7.50 $\frac{\gamma-Fe_2O_3}{volume}$ | 3.57 $\frac{\gamma-Fe_2O_3}{volume}$ + 1.78 $\frac{Mn_3O_4}{volume}$ | 3.18 $\frac{\gamma-Fe_2O_3}{volume}$ + 1.98 $\frac{Mn_3O_4}{volume}$. Recast in terms of a composite ferrite structure this becomes $(Mn_XFe_{1-X})_3O_{4.3}$, where X ranges from 0.42 to 0.47 for inner and outer shell regions, respectively. This is surprisingly close to the previously extracted X of 0.40 to 0.46 using Fe_3O_4 and γ-Mn_2O_3 as inputs. Our conclusion is that the extracted scattering profile shapes and corresponding chemical compositions are largely independent of oxide inputs used.

Non-Diffractive Measurement Comparisons

Size Distribution via TEM: The overall diameter of the core|shell nanoparticles obtained from TEM, Fig. 5a-c, of 8.0 $\pm$ 1.9 nm corresponds satisfactorily with ASAXS analysis at 8.2 $\pm$ 0.2 nm. On the other hand, the size of the uncoated Fe_3O_4 cores obtained from ASAXS ($\approx$ 0.8 nm) is remarkably small since the original Fe_3O_4 seeds used are 6.5 $\pm$ 1.1 nm (see Fig. 5a,c). The reduction in diameter of the pure Fe_3O_4 core regions within the core|shell particles from that of the uncoated Fe_3O_4 seeds indicates that some of the Fe_3O_4 reacts with the γ-Mn_2O_3 and is incorporated in a mixed-metal outer shell, as has been observed for similar particles.[27,36] In fact, the degree of interdiffusion between Mn and Fe and the exact Mn-oxide phase in this type of nanoparticles depends critically on the temperature at which the nanoparticles are exposed to air and on the size of the nanoparticles.[27,36,42] The presence of uncoated Fe_3O_4 seeds evidenced by the bimodal distribution of Fe_3O_4 nanoparticles in the ASAXS analysis is not obvious from the TEM analysis. However, it may explain the unusually large increase in log-normal standard deviation in the core|shell nanoparticles with respect to the original seeds (see Fig. 5c). In fact, closer

inspection of the particle size distribution of the core|shell nanoparticles reveals an asymmetric tail of the distribution towards smaller sizes. This part of the distribution might be associated with the uncoated Fe_3O_4 nanoparticles, which according to ASAXS, are much smaller ($\approx$ 2.2 nm to 3.4 nm) than the mean size of the seeds (6.5 nm). Accordingly, Ostwald ripening is likely the mechanism by which the relatively larger core|shell nanoparticles grow at the expense of the smaller ones thereby redissolving the manganese oxide shell from the small seeds,[43] although traces of Mn on the uncoated seeds cannot be ruled out.

Core|Shell Evidence via EELS: The quantitative analysis of the local composition of the core|shell nanoparticles using EELS reveals a multilayered structure with an Fe-based core and a Mn-rich shell, Fig. 6a, shown for a collection of particles. Quantitatively, EELS yields a 2.5 nm (core radius) Fe_3O_4 |1 nm (inner shell) $MnFe_2O_4$|0.5 nm (outer shell) γ-Mn_2O_3. This is in qualitative agreement with the ASAXS core|graded-shell structure, where both approaches clearly show the presence of an intermixed shell structure and a reduced core size (with respect to the seeds). Nevertheless, the ASAXS analysis indicates a more delocalized distribution of the Fe compared with the EELS results. However, it is important to emphasize that the EELS results are based on a handful of nanoparticles, while ASAXS measures the ensemble-average.

Spectroscopic Techniques: Fe-rich regions of MnxFe3-xO4 (MnFe2O4-Fe3O4) form a cubic spinel, while Mn-rich regions of FexMn3-xO4 (FeMn2O4-Mn3O4) form a tetragonal spinel. High resolution scanning tunneling electron microscopy (HR-STEM), Fig. 6a-b, indicate that two, distinctive crystalline phases co-exist within the same nanoparticle. Longer-ranged x-ray diffraction (XRD), Fig. 6c, also reveals the existence of (Fe-rich) cubic and (Mn-rich) tetragonal phases. The ratio of intensities between the tetragonal and cubic phases from XRD is in concordance with a core|shell structure with a cubic spinel core and a thin tetragonal spinel shell. Electron spin resonance (ESR) produces distinctive resonances, β and ξ, as a function of the temperature (details in supplementary material). The more intense β line broadens and shifts towards a lower field as the temperature decreases and is qualitatively similar to the spectra reported for Fe_3O_4 nanoparticle systems,[44–46] while the ξ linewidth remains almost unchanged down to 50 K and broadens be-

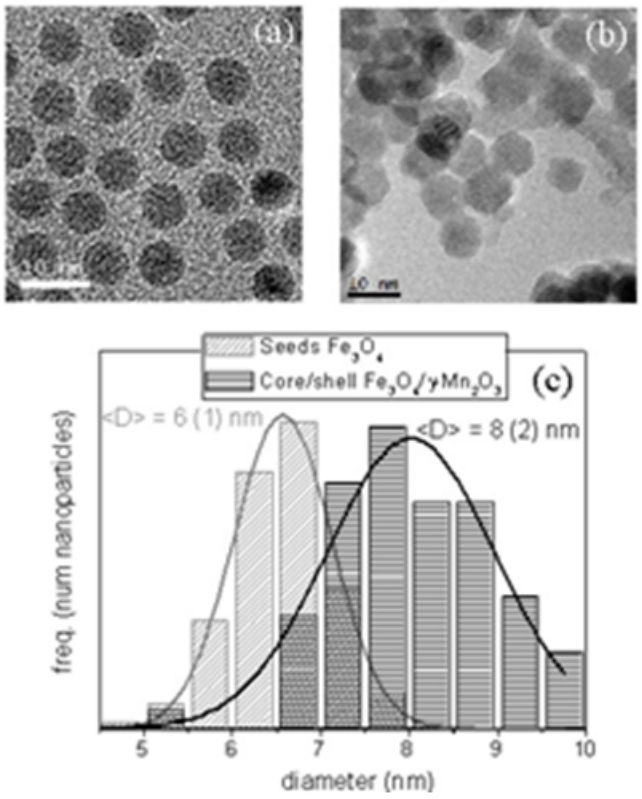

Figure 5: TEM image of (a) the Fe_3O_4 seeds and (b) the $Fe_3O_4|\gamma$-Mn_2O_3 core|shell nanoparticles. (c) Particle size distribution comparing the particles in (a) and (b). The lines show the fit of the experimental data to a log-normal distribution. The values given in the figure correspond to the mean value and the log-normal standard deviation.

low this, consistent with either Mn_3O_4[47–49] or a $Mn_xFe_{3-x}O_4$ spinel.[50] XAS and x-ray magnetic circular dichroism (XMCD) indicate that the Fe exists in a near single crystalline, whereas the Mn exists in mixed oxidation states corresponding to multiple crystalline phases (supplementary section). These complementary measurements indicate the presence of multi-crystalline phases, consistent with the ASAXS modeling results of a $(Mn_XFe_{1-X})_3O_4$ core|shell|shell morphology with increasing Mn content toward the surface.

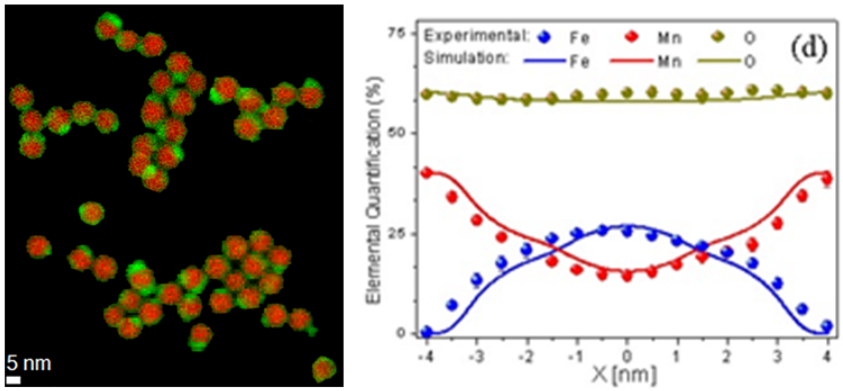

Figure 6: (a) EELS Fe (red) and Mn (green) elemental imaging. (b) Averaged Fe, Mn and O elemental quantification and a simulation considering a 2.5 nm (radius) Fe_3O_4 core|1 nm $MnFe_2O_4$|0.5 nm γ-Mn_2O_3.

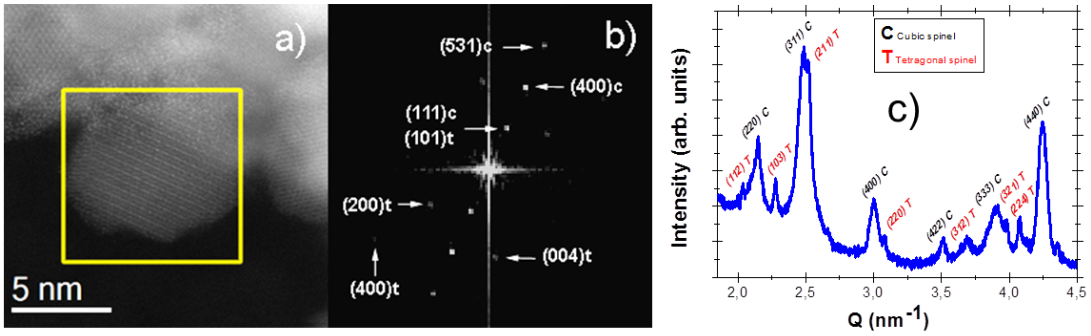

Figure 7: (a) HR-STEM image for the core|shell nanoparticle and (b) the FFT of the highlighted in (a). (c) X-ray diffraction. Cubic spinel and tetragonal spinel structures, are labeled as c and t, respectively.

Conclusions

In summary, we have demonstrated that multiple-energy ASAXS provides significant enhancement in sensitivity to internal material boundaries of layered nanoparticles compared with the traditional modeling of a single scattering energy, even for cases in which high scattering length density (ρ) contrast between the constituent materials exists. Applied to a system of nominal core|shell Fe_3O_4|γ-Mn_2O_3 nanoparticles, this technique revealed that the core|shell nanoparticles are comprised of a graded nanoparticle tending toward Fe_3O_4 at the center, yet retaining a significant portion of Fe out to the exterior. The average Fe-Mn-oxide shell composition can be recast in terms of a ferrite structure as $(Mn_XFe_{1-X})_3O_{\approx 4}$ with X ranging from 0.40 (interior shell of diameter 0.8 nm to 4.8 nm) to 0.46 (exterior shell of diameter 4.8 nm to 8.2 nm). The presence of a small fraction of uncoated Fe_3O_4 seeds explains the smearing of the Fe_3O_4 scattering contribution without assigning undue polydispersity. The model-derived concept of a dual distribution of core|shell nanoparticles plus uncoated seeds is further corroborated by both a shift in low-Q peak placement at the Fe K-edge and a measurable difference between structure factors $S_{Fe_3O_4}$ and $S_{\gamma-Mn_2O_3}$ obtained from analysis of the derived interference term, $\mathfrak{F}_{Int1}$. These fine details revealed through the direct contrast of the material specific scattering profiles simply could not have been obtained from simultaneous fitting of the resonant data as is generally practiced. The results, although they are in concordance with TEM, EELS, HR-STEM, ESR, XAS, and XMCD analysis, evidence further ensemble-averaged structural details which would have been difficult to access using solely these studies. Given how dependent core|shell nanoparticle behavior and functionality often are on internal structure, multi-energy ASAXS shows great promise in the rapidly developing field of nanoparticle research.

Acknowledgement

This work utilized facilities supported in part by the National Science Foundation under Agreement No. DMR-0944772 and DMR-0454672. U.S. department of Energy Contract No. DE-AC02-06CH11357, and Ames Laboratory Contract No.W-7405-Eng-82. Work supported by the Span-

ish MICINN (MAT2008-01939-E, MAT2010-20616-C02, MAT2010-16407, CSD2009-00013 and CSD2006-00012), and Catalan DGR (2009-SGR-1292 and 2009-SGR-00035). GSA thanks the Wallenberg Wood Science Center for the partial financial support. MDB was partially supported by an ICREA ACADEMIA award. Finally, we give special thanks to D. Robinson, P. Ryan, and Z. Islam of Argonne National Laboratory for their efforts in making our experiment successful.

Supporting Information Available

Synthesis. The synthesis of the onion particles was carried out following a multistep procedure where preformed iron oxide nanoparticles were used as seeds for the subsequent growth of manganese (II) oxide and its passivation to form γ-Mn_2O_3.[36] Briefly, an iron (III) oleate precursor was prepared following a similar procedure reported earlier.[51] 14 mmol of iron (III) chloride ($FeCl_3 \cdot 6H_2O$, 97 %, Aldrich), and 42 mmol of sodium oleate (NaOl, Riedel-de Haën) were dissolved in 21 mL ethanol (99.5 %, Panreac), 28 mL deionized water, and 50 mL hexane (Fluka) and refluxed under magnetic stirring for 3 hours. During this time it is possible to see that the precursor changes from a light red color to a burgundy red, indicating the formation of the precursor. The organic phase was washed with 5 mL of deionized water three times and dried under vacuum. In a typical synthesis, spheroidal particles with a particle diameter D = 6.5 nm $\pm$ 1.1 nm were prepared by dissolving 3 mmol of the precursor, 3 mmol of oleic acid (OlOH, Aldrich) in 36 mL of 1-octadecene (ODE 90 %, Aldrich) at 70 ^{o}C. The mixture was heated to 320 ^{o} (at 5 ^{o}C/min) under stirring at 130 rpm and kept for 30 min. The reaction vessel was allowed to cool down to room temperature before exposure to air. The particles were retrieved by several cycles of centrifugation at 2000xg, disposal of supernatant, re-dispersion in hexane and coagulation with ethanol.

The manganese oxide layers were laid on the iron oxide-based nanoparticles modifying an earlier reported procedure used for the synthesis of MnO|γ-Mn_2O_3 nanoparticles.[42,52] The procedure is as follows: 30 mg of iron oxide seeds, 2.3 mmol of 1,2-hexadecanediol (HDD, Aldrich) and 1.9 mmol of manganese (II) acetylacetonate ($Mn(acac)_2$, Aldrich) were added to 150 mL of benzylether (Bz_2O, Fluka) together with 5 mL (16 mmol) of oleic acid (OlOH, Aldrich) and 50 mL

of oleylamine (OlNH2, Fluka). The slurry was de-aerated with Ar for 15 min. The slurry was then heated at $\sim 7\ ^{o}$C/min to 200 ^{o}C, allowed to proceed under reflux with a residence time, t $\sim$ 60 min and then removed from the heating source and allowed to cool to room temperature. The particles were washed from the reaction media by subsequent steps of precipitation under ethanol, centrifugation, and re-dispersion in hexane.

Small Angle Neutron Scattering (SANS). SANS patterns collected at room temperature at the NIST Center for Neutron Research beam line NG3. The incident wavelength was 0.5 nm with 11 % wavelength spread.

Anomalous Small Angle X-ray Scattering (ASAXS). SAXS patterns were measured at room temperature at the Mn and Fe K-edges (6535 eV and 7112 eV, respectively)[41] and off-resonance (6000 eV) at the Advanced Photon Source beam line 6-ID-B. The scattering data were collected using a SII Nano Technology Vortex detector[53] with an energy discrimination of 134 eV, while the incident beam intensity was monitored using a high voltage ion chamber. The detector/monitor response was calibrated as a function of incident x-ray energy by measuring the fluorescence produced by a vanadium thin film (with its own well-known energy response curve[41]) over the range of 6.0 keV to 9.0 keV. The absorption of the nanoparticles was measured via direct beam transmission at each energy, and corrected for in the data normalization.

Transmission electron microscopy (TEM). TEM images were obtained using a JEM-2100[53] with a LaB_6 filament and a JEM-2010F[53] with a field-emission gun operating at 200 kV, the latter equipped with a post-column Gatan Image Filter (GIF) energy spectrometer.

High Resolution scanning tunneling electron microscopy (HR-STEM) and Electron energy loss spectra (EELS).

HR-STEM and EELS have been obtained in a FEI Titan Low-base[53] operating at 300 kV (HR-STEM). The indexing of the FFT of HR-STEM image (Fig. 6) reveals the presence of two different crystallographic phases, related to iron oxide cubic spinel phase (JCPDS Card No. 82-1533) in the core and manganese oxide tetragonal spinel (JCPDS Card No. 24-0734) in the shell, hence confirming the core|shell character of the nanoparticles.

EELS were acquired at different positions along the diameter of the nanoparticles on the L-edge of Mn and Fe with an energy resolution of 0.8 eV. The quantitative analysis of the EELS spectra was performed using the home-made software package MANGANITAS..[53–55] Figure Figure 8 shows EEL spectra at the Mn-and Fe-edges taken in the same area at different magnifications (see top). As can be seen, the ratio of intensities between the different EELS peaks in the respective spectra is roughly independent of the magnification, indicating that the overall composition of the sample is approximately the same for a handful of particles (highest magnification), tens of particles (medium magnification) or for hundreds of particles (lower magnification).

X-ray Diffraction (XRD).

XRD patterns were collected using a Panalytical X'Pert Pro diffractometer[53] with Cu Kα radiation.

Electron spin resonance (ESR).

ESR measurements were performed in an ESP$-$300 Bruker spectrometer,[53] operating at a frequency $\nu \sim$9.5 GHz (X$-$band), and in the 3$-$ 300 K temperature range. In order to avoid spurious signals, care was taken to not saturate the cavity due to the giant ESR sample signal. For this purpose, and to ensure good penetration of the microwaves into the sample, the $Fe_3O_4/\gamma-Mn_2O_3$ nanoparticles were diluted in a non absorbing KCl salt. No noticeable changes of the cavity coupling were registered in the whole set of experiments. From the ESR spectra we derived the resonance field H_r, the peak to peak linewidth ΔH and the ESR intensity. From the resonance condition: $h\nu = g\mu_B H_r$ (where h and μ_B are the Plank constant and the Bohr magneton respectively), the gyromagnetic $g-$factor was obtained, and the spectrum intensity is the area under the absorption curve. As the materials studied in this work are powder samples the observed spectra are inhomogeneous broadening due to the angular, size and shape distribution.

Figure Figure 9 shows the ESR spectra of the $Fe_3O_4/\gamma-Mn_2O_3$ system at different temperatures. At first glance, it is observed that the ESR spectra have the contribution of several lines identified as α, β, ξ and δ. The ESR parameters of these lines are very different indicating the presence edof different magnetic species.

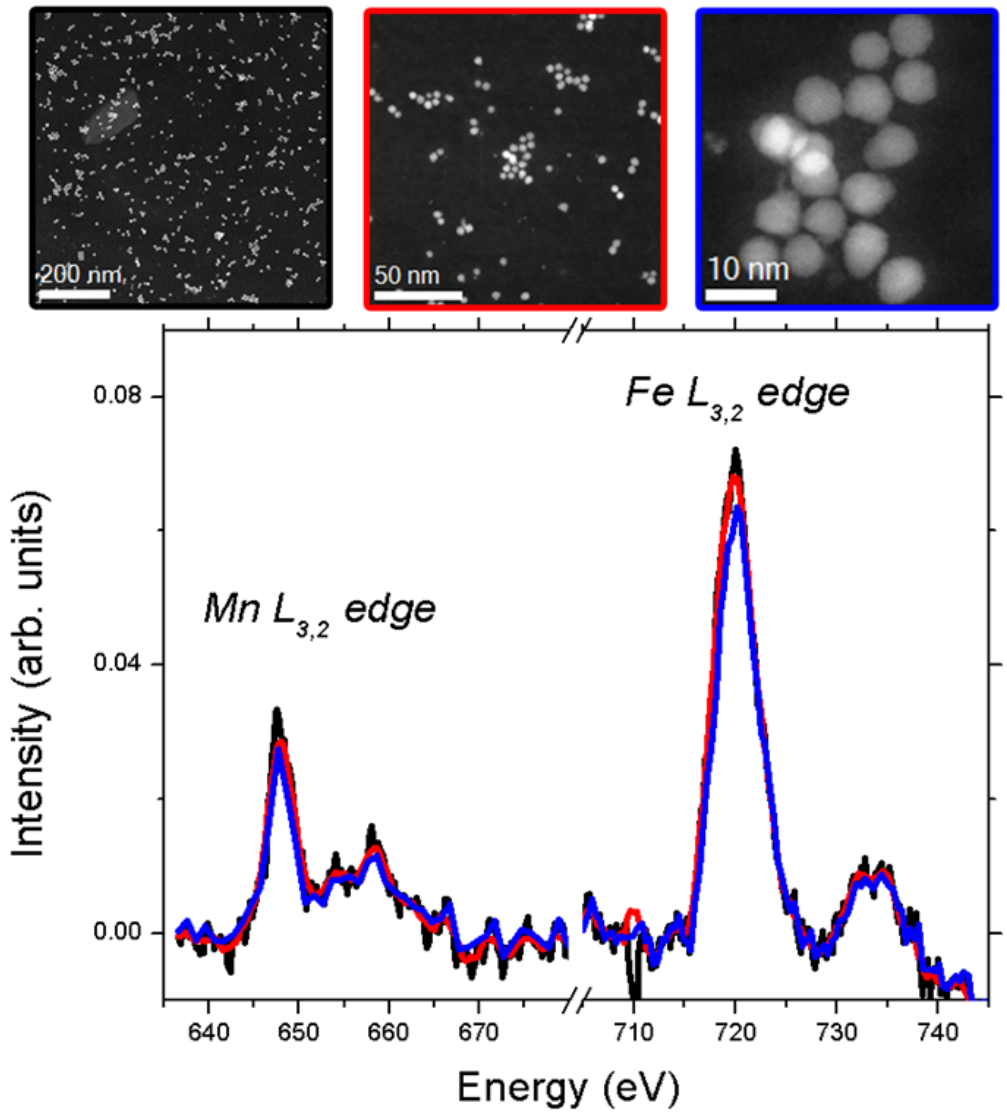

Figure 8: EEL spectra taken at different STEM magnifications show a consistent ratio of Fe to Mn across the nanoparticles.

The low field resonance (α- line) is located at $H_r \sim$1600 Oe, from this value the gyromagnetic ratio was calculated, resulting $g = 4.23$ (8). The $g =30/7\sim4.3$ resonance is a typical signal observed for ${}^6S_{5/2}$ ions (Fe^{3+} or Mn^{2+}) in glasses and can be understood in terms of the crystal field interaction of the magnetic ions located in an *orthorhombic distorted site*. ([50,56,57]) It is noteworthy that the intensity of the line does not follow the paramagnetic $1/T$ dependence. This behavior was observed in other nanoparticles system, where the paramagnetic resonance was ascribed to surface ions.[58] Considering that the paramagnetic intensity is proportional to the number of resonant ions, the decrease of the paramagnetic ions is correlated to the growth of the magnetically ordered core, when the temperature decreases. Therefore the α- line of the $Fe_3O_4/\gamma{-}Mn_2O_3$ system could be associated to the paramagnetic resonance of Fe^{3+} and Mn^{2+} surface ions. When the temperature diminishes the thermal fluctuations are reduced and the surface ions may coupled to the magnetically ordered phase, as a consequences the paramagnetic signal diminishes.

The second line ($\delta-$line) is centered at $g = 2.024$ (2) down to the lowest measured temperature and increases its intensity as $1/T$ when the temperature decreases. The described behavior is consistent with a paramagnetic resonance and could be associated to Fe^{3+} or Mn^{2+} ions located in more symmetric sites(i.e. sites with cubic or tetragonal symmetry).[59]

The β and ξ resonances show important variation of their ESR parameters as a function of the temperature. At room temperature the $\beta-$resonance is an inhomogeneous broadening line, $\Delta H =$870 Oe, centered at $g = 2.08$ (4). When the temperature diminishes the resonance broadens and shifts towards a lower field. Figure Figure 10 shows the temperature evolution of both the H_r and ΔH parameters. Instead the $\xi-$resonance corresponds to a narrow line overlapped with the $\beta-$resonance. The thin signal is better resolved at low temperature when the $\beta-$resonance is broaden; for example at $T =$185 K is centered at $g =$2.2 (1) and $\Delta H =$ 200 Oe. From Fig. Figure 10 it is observed that the resonance field shifts toward lower field values when the temperature decreases. Meanwhile the linewidth remains almost unchanged down to 50 K and at lower temperature ΔH broadens. As was mentioned above, the different values and temperature dependence of the ESR parameters indicate that the β and ξ lines correspond to different magnetic species. Be-

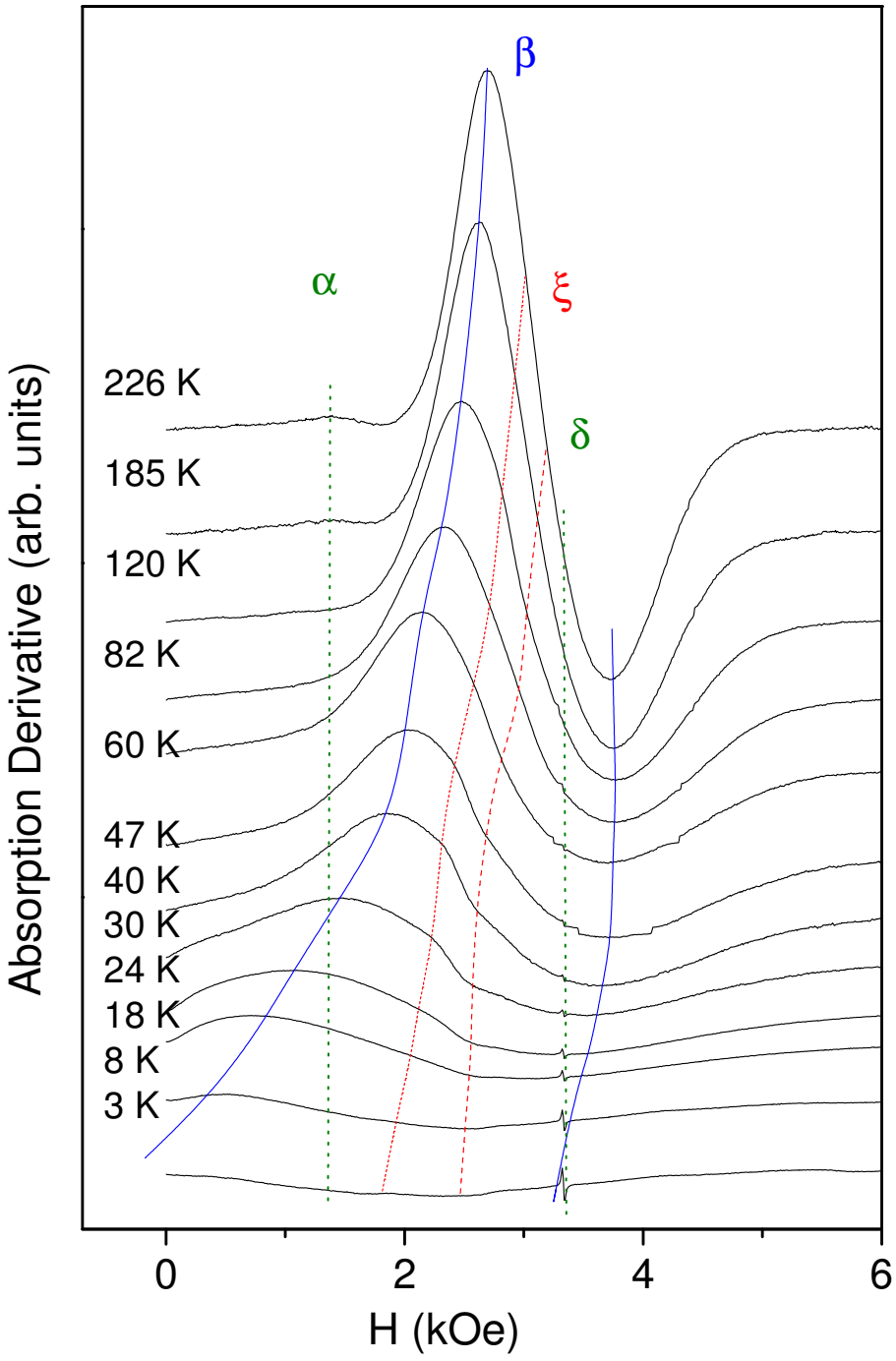

Figure 9: ESR spectra of $Fe_3O_4/\gamma{-}Mn_2O_3$ core/shell nanoparticles system at different temperatures. The spectra are vertically shifted for clarity. Notice that the ESR absorption has the contribution of four resonance, named α, β, ξ and δ. The dotted (green) lines signal H_r of the α and δ lines; and the solid (blue) and dashed (red) lines signal ΔH for the β and ξ resonance, respectively.

sides, the remarkable change of H_r with the temperature indicate the presence of important internal effective fields in both phases.

In particular the more intense $\beta-$resonance is qualitatively similar to the spectra reported for Fe_3O_4 nanoparticles system.[44–46] For Fe_3O_4 superparamagnetic nanoparticles an inhomogeneous broadening in the ferromagnetic resonance spectrum is observed with a monotonous increasing of ΔH, while H_r decreases when the temperature diminishes. Below the transition temperature the resonance condition changes by the presence of effective anisotropy fields (H_a), as a consequence the resonance field decreases by H_a from the paramagnetic resonance field value.[60] In nanoparticles systems, the effective anisotropy field usually increases when the temperature diminishes, then a monotonous decrease of H_r is observed.[44,50] Besides, the observed peak to peak linewidth of powder sample results from the angular distribution of anisotropy axis and the contribution of the intrinsic linewidth.[60,61] Both terms enlarge ΔH when the temperature diminishes. The reported ESR parameter values and their described temperature dependence are consistent with the observed behavior of the $\beta-$resonance, therefore we assign this line to Fe_3O_4 nanoparticles.

On the other hand, the fact that the linewidth of the narrow $\xi-$line remains almost unchanged down to 50 K could indicate that this resonance correspond to a paramagnetic phase which ferrimagnetically orders at lower temperature, in accordance to the ΔH widening. This behavior resembles the results reported for Mn_3O_4 oxides.[47–49] The resonance field variation could be explained by the presence of internal field originated by the ordered $\beta-$phase (assigned to the Fe_3O_4) which influences the $\xi-$resonance. Similar response is observed when Gd ions are used as intrinsic local probes to sense the internal magnetic field of a sample.[62] To our knowledge, there are scarce works in the literature related to the ESR spectroscopy on $Mn_xFe_{3-x}O_4$ spinels. Kliava et al.[50] report the ESR results of superparamagnetic nanoparticles system with structure close to $MnFe_2O_4$. This work reports a single line ($\Delta H \sim$230 Oe) centered at $g \sim$2 at room temperature, that monotonously increases when the temperature decreases. Taking into account these results the observed $\xi-$ line is consistent with a Mn_3O_4 or $Mn_xFe_{3-x}O_4$ spinel with $T_C \sim$ 50 K.

Finally it is worthy to remark that the $\gamma-Mn_2O_3$ phase is unlikely to be detected by ESR due

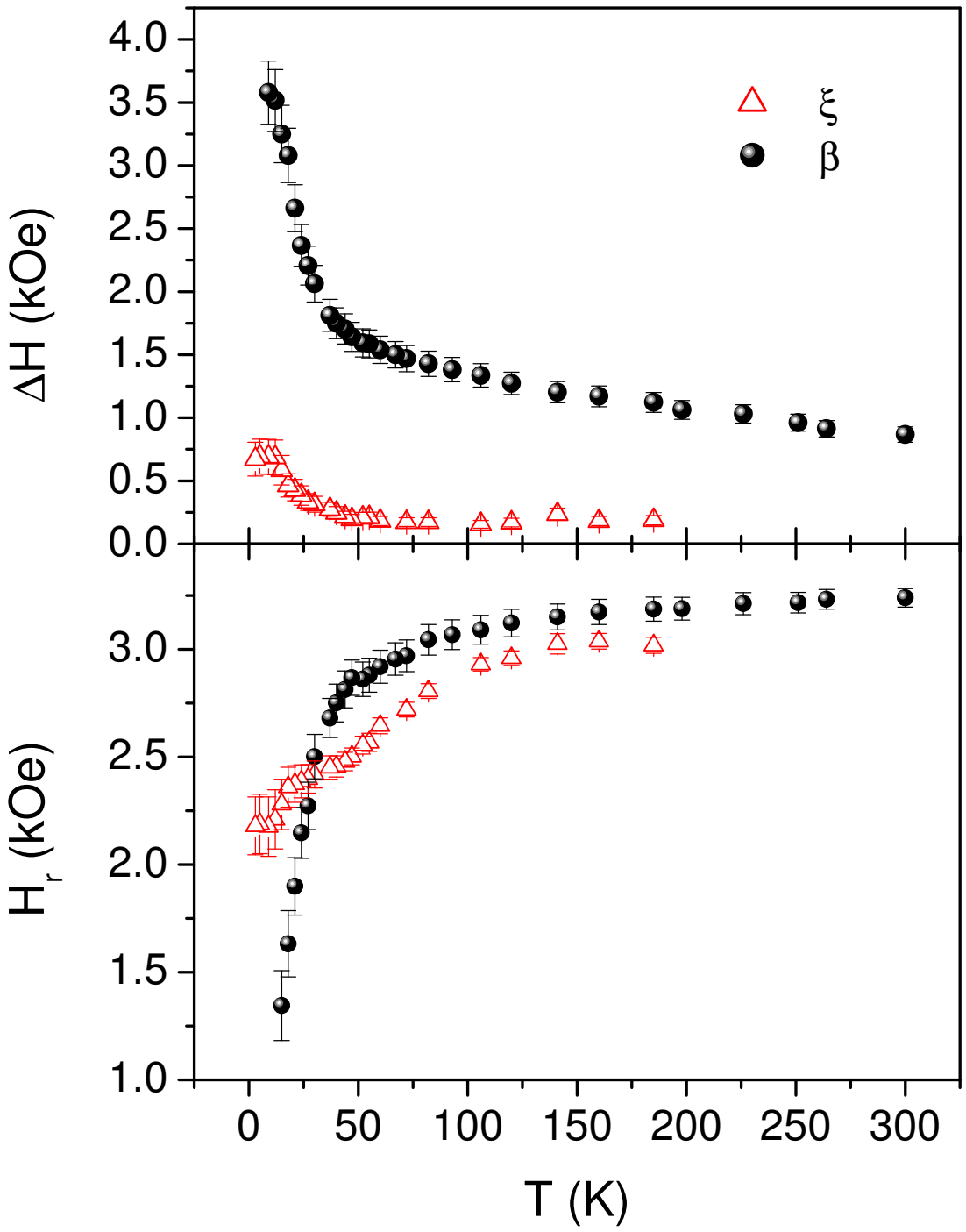

Figure 10: (ΔH) and resonance field (H_r) as a function of the temperature of the β and ξ resonances.

to the large spin−lattice relaxation of Mn^{3+}, and consequently the ESR linewidth is larger than 3 kOe at room temperature[63] or could not be resolved.[49] In summary, from the ESR results we can distinguished in the core/shell nanoparticle system the presence of superparamagnetic Fe_3O_4 phase plus the resonance signal of a second magnetic phase that could be associated to Mn_3O_4 or $Mn_xFe_{3-x}O_4$. Besides Fe^{3+} and Mn^{2+} surface ions are detected which are paramagnetic at room temperature and coupled to the magnetic ordered phase when the temperature decreases.

X-ray Absorption Spectroscopy (XAS) and X-ray Magnetic Circular Dichroism (XMCD).

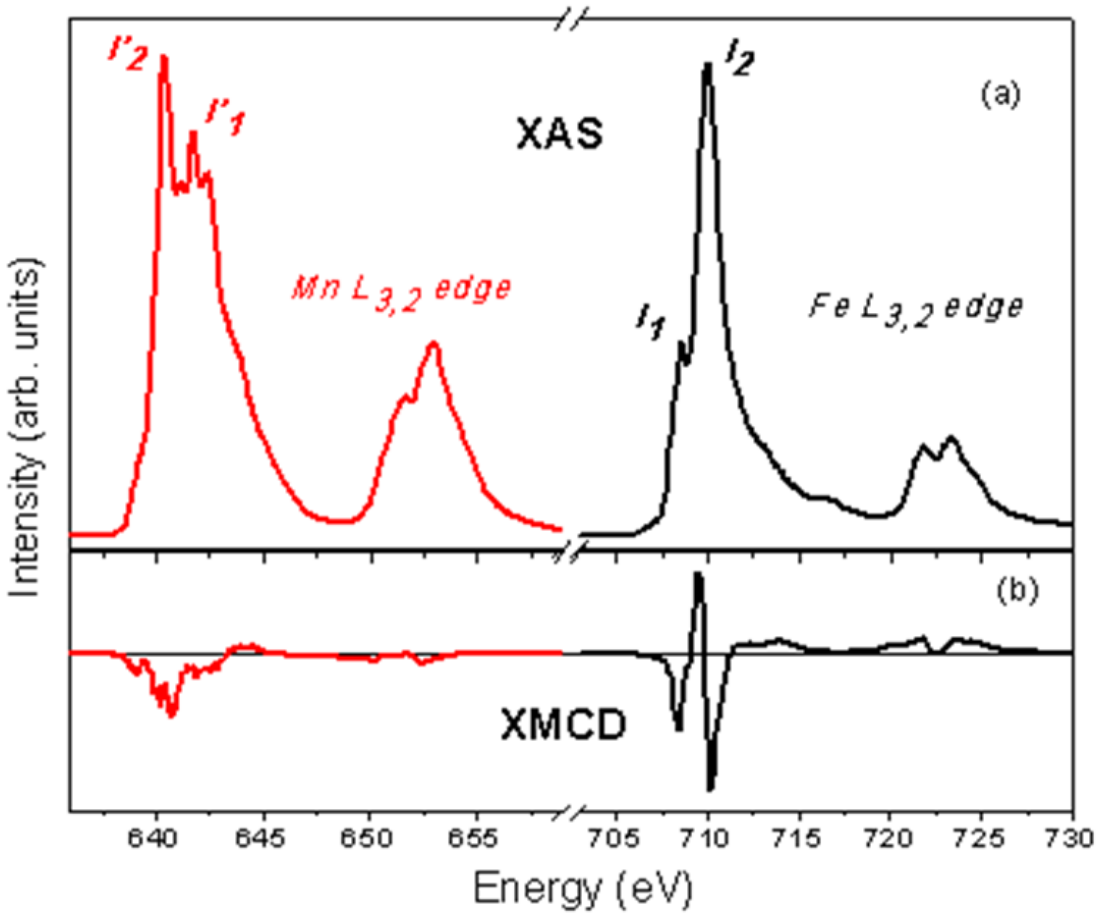

Figure 11: XAS (top) and XMCD (bottom) spectra at the (left) Mn and (right) Fe edges of core|shell nanoparticles.

XAS and XMCD measurements were performed on dried core|shell nanoparticles spread onto carbon tape at the SIM beamline of the Swiss Light Source (SLS) of the Paul Scherrer institute.

Both XAS and XMCD spectra were recorded at the Fe and Mn $L_{3,2}$ edges using total electron yield (TEY) mode at 10 K in a magnetic field of 5 Tesla after field cooling (FC) from 300 K under an applied field of 5 Tesla. The XMCD signal was normalized by the area of the XAS spectra after correcting for the background.

Figure Figure 11 shows the XAS and XMCD spectra obtained at the Fe and Mn $L_2, 3$ edges for the core|shell sample. From the Fe-edge spectrum it can be seen that the ratio of intensities between the I_1 and I_2 peaks, I_1/I_2, is 0.4. For Fe_3O_4 and γ-Fe_2O_3 this ratio is 0.53 and 0.19,[64] respectively. Hence, it can be inferred that the sample has an intermediate composition between γ-Fe_2O_3 and Fe_3O_4. Given that I_1 can be associated to the presence of Fe^{2+} in octahedral (Oh) positions while I_2 correlates to Fe^{3+} ions located in Oh and tetrahedral (Td) environments, and given that $(Fe^{3+})Td[Fe^{3+}Fe^{2+}]OhO_4$ (*i.e.* Fe_3O_4), and $(Fe^{3+})Td[Fe^{3+}_{5/3}Fe^{3+}_{1/3}]OhO_3$ (*i.e.* γ-Fe_2O_3) structures, the presence of a $(Fe^{3+})Td[Fe^{3+}Mn^{2+}]OhO_4$ phase (*i.e.* $MnFe_2O_4$)[65] without Fe^{2+} ions in octahedral positions would be consistent with the experimental I_1/I_2 ratio. On the other hand the XAS spectrum at the Mn $L_2, 3$ edge resembles that of pure tetragonal $(Mn^{2+})Td[Mn^{3+}]Oh_2O_4$ (i.e Mn_3O_4).[66] However, it has a lower intensity ratio, $I'_1/I'_2 = 0.7$, than expected for Mn_3O_4, *i.e.*, $I'_1/I'_2 = 0.87$, but larger than the corresponding for $MnFe_2O_4$, $I'_1/I'_2 = 0.5$.[67] Hence, the Mn $L_2, 3$ signal can be understood as a mixed signal arising both from the Mn-rich shell of tetragonal $(Mn_X xFe_{1-X})_3O_4$ phase, and the intermediate shell with a cubic $(Mn_X xFe_{1-X})_3O_4$ structure. Note that since the total electron yield (TEY) mode depends strongly on the probing depth, (λ_X), which for soft X-ray can be taken to be of the order of 10 nm for most of metal oxides,a quantitative analysis of the XAS results is rather complex.

Concerning the XMCD spectra, the results at the Fe-edge are similar to those of pure cubic spinel iron oxides (Fe_3O_4 and γ-Fe_2O_3) spectra,[68] although some small deviations attributed the presence of the mixed $(Mn_X xFe_{1-X})_3O_4$ oxide can be observed. Particularly, the different intensity peak ratio of the two first peaks of the iron XMCD signal with respect to pure iron oxides can be interpreted in the same way as XAS analysis regarding the concentration of Fe^{2+} ions in octahedral positions.[67,69] In contrast, the spectrum at the Mn-edge cannot be associated to any single phase

and is obviously attributed to a mixed XMCD signal, *e.g.* arising from two (or more) different Mn-oxide structures.[66]

This material is available free of charge via the Internet at `http://pubs.acs.org/`.

References

(1) Kallinteri, P.; Higgins, S.; Hutcheon, G. A.; St. Pourçain, C. B.; Garnett, M. C. *Biomacromolecules* **2005**, *6*, 1885–1894.

(2) Davis, M. E.; Chen, Z.; Shin, D. M. *Nat. Rev. Drug Discov.* **2008**, *7*, 771–782.

(3) Frey, N. A.; Peng, S.; Cheng, K.; Sun, S. *Chem. Soc. Rev.* **2009**, *38*, 2532–2542.

(4) Sharma, R.; Chen, C. *J. Nanopart. Res.* **2009**, *11*, 671–689.

(5) Mishra, B.; Patel, B. B.; Tiwari, S. *Nanomed. Nanotechnol. Biol. Med.* **2010**, *6*, 9–24.

(6) Costi, R.; Saunders, A.; Banin, U. *Angew. Chem. Int. Ed.* **2010**, *49*, 4878–4897.

(7) Carbone, L.; Cozzoli, P. D. *Nano Today* **2010**, *5*, 449–493.

(8) Schärtl, W. *Nanoscale* **2010**, *2*, 829–843.

(9) Ijiri, Y.; Kelly, C. V.; Borchers, J. A.; Rhyne, J. J.; Farrell, D. F.; Majetich, S. A. *Appl. Phys. Lett.* **2005**, *86*, 243102.

(10) Kechrakos, D.; Trohidou, K.; Vasilakaki, M. *J. Magn. Magn. Mater.* **2007**, *316*, e291–e294.

(11) Golosovsky, I. V.; Salazar-Alvarez, G.; López-Ortega, A.; González, M. A.; Sort, J.; Estrader, M.; Suriñach, S.; Baró, M. D.; Nogués, J. *Phys. Rev. Lett.* **2009**, *102*, 247201.

(12) Inderhees, S. E.; Borchers, J. A.; Green, K. S.; Kim, M. S.; Sun, K.; Strycker, G. L.; Aronson, M. C. *Phys. Rev. Lett.* **2008**, *101*, 117202.

(13) Berkowitz, A. E.; Rodriguez, G. F.; Hong, J. I.; An, K.; Hyeon, T.; Agarwal, N.; Smith, D. J.; Fullerton, E. E. *Phys. Rev. B* **2008**, *77*, 024403.

(14) Elder, S. H.; Cot, F. M.; Su, Y.; Heald, S. M.; Tyryshkin, A. M.; Bowman, M. K.; Gao, Y.; Joly, A. G.; Balmer, M. L.; Kolwaite, A. C.; Magrini, K. A.; Blake, D. M. *J. Am. Chem. Soc.* **2000**, *122*, 5138–5146.

(15) Peng, S.; Lei, C.; Ren, Y.; Cook, R. E.; Sun, Y. *Angew. Chem. Int. Ed.* **2011**, *50*, 3158–3163.

(16) Song, J.-H.; Atay, T.; Shi, S.; Urabe, H.; Nurmikko, A. V. *Nano Letters* **2005**, *5*, 1557–1561.

(17) Joo, S. H.; Park, J. Y.; Tsung, C.-K.; Yamada, Y.; Yang, P.; Somorjai, G. A. *Nat. Mater.* **2009**, *8*, 126–131.

(18) Bruchez Jr., M.; Moronne, M.; Gin, P.; Weiss, S.; Alivisatos, A. P. *Science* **1998**, *281*, 2013–2016.

(19) Brodbeck, C. M.; Bukrey, R. R. *Phys. Rev. B* **1981**, *24*, 2334.

(20) Trudel, S.; Jones, C. H. W.; Hill, R. H. *J. Mater. Chem.* **2007**, *17*, 2206.

(21) Rojas, T. C.; Sayagues, M. J.; Caballero, A.; Koltypin, Y.; Gedanken, A.; Ponsonnet, L.; Vacher, B.; Martin, J. M.; Fernandez, A. *J. Mater. Chem.* **2000**, *10*, 715–721.

(22) Cho, S.; Idrobo, J.; Olamit, K., J.and Liu; Browning, N.; Kauzlarich, S. *Chem. Mater.* **2005**, *17*, 3181–3186.

(23) Teng, X.; Yang, H. *Nanotechnology* **2005**, *16*, S554–S561.

(24) Bao, Y.; Calderon, H.; Krishnan, K. M. *J. Phys. Chem. C* **2007**, *111*, 1941–1944.

(25) Wang, J. X.; Inada, H.; Wu, L.; Zhu, Y.; Choi, Y.; Liu, P.; Zhou, W.-P.; Adzic, R. R. *J. Am. Chem. Soc.* **2009**, *131*, 17298–17302.

(26) Vonk, C. G. *J. Appl. Cryst.* **1976**, *9*, 433–440.

(27) Estradé, S.; Yedra, L.; López-Ortega, A.; Estrader, M.; Salazar-Alvarez, G.; Baró, M.; Nogués, J.; Peiró, F. *Micron* **2012**, *43*, 30–36.

(28) Rieker, T.; Hanprasopwattana, A.; Datye, A.; Hubbard, P. *Langmuir* **1999**, *15*, 638–641.

(29) Koh, A. L.; Bao, K.; Khan, I.; Smith, W. E.; Kothleitner, G.; Nordlander, P.; Maier, S. A.; McComb, D. W. *ACS Nano* **2009**, *3*, 3015–3022.

(30) Karle, J. *Acta Crystallogr. Sect. A* **1984**, *40*, 1–4.

(31) Hendrickson, W. A. *Science* **1991**, *254*, 51–58.

(32) Stauber, D. J.; DiGabriele, A. D.; Hendrickson, W. A. *Proc. Natl. Acad. Sci.* **2000**, *97*, 49–54.

(33) Miao, J.; Charalambous, P.; Kirz, J.; Sayre, D. *Nature* **1999**, *400*, 342–344.

(34) Barnardo, T.; Hoydalsvik, K.; Winter, R.; Martin, C. M.; Clark, G. F. *J. Phys. Chem. C* **2009**, *113*, 10021–10028.

(35) Haug, J.; Kruth, H.; Dubiel, M.; Hofmeister, H.; Haas, S.; Tatchev, D.; Hoell, A. *Nanotechnology* **2009**, *20*, 505705.

(36) Salazar-Alvarez, G.; Lidbaum, H.; López-Ortega, A.; Estrader, M.; Leifer, K.; Sort, J.; Suriñach, S.; Baró, M. D.; Nogués, J. *J. Am. Chem. Soc.* **2011**, *133*, 16738–16741.

(37) Kline, S. R. *J. Appl. Cryst.* **2006**, *39*, 895–900.

(38) DeTitta, G. T.; Weeks, C. M.; Thuman, P.; Miller, R.; Hauptman, H. A. *Acta Crystallogr. Sect. A* **1994**, *50*, 203–210.

(39) Weeks, C. M.; DeTitta, G. T.; Hauptman, H. A.; Thuman, P.; Miller, R. *Acta Crystallogr. Sect. A* **1994**, *50*, 210–220.

(40) Materlik, G., Sparks, C. J., Fischer, K., Eds. *Resonant Anomalous X-Ray Scattering: Theory and Applications*; Elsevier: North-Holland, 1994.

(41) Henke, B.; Gullikson, E.; Davis, J. *Atomic Data and Nuclear Data Tables* **1993**, *54*, 181–342.

(42) López-Ortega, A.; Tobia, D.; Winkler, E.; Golosovsky, I. V.; Salazar-Alvarez, G.; Estradé, S.; Estrader, M.; Sort, J.; González, M. A.; Suriñach, S.; Arbiol, J.; Peiró, F.; Zysler, R.; Baró, M. D.; Nogués, J. *J. Am. Chem. Soc.* **2010**, *132*, 9398–9407.

(43) Li, Q.; Wang, J.; He, Y.; Liu, W.; Qiu, X. *Cryst. Growth Des.* **2009**, *9*, 3100–3103.

(44) Pal, S.; Dutta, P.; Shah, N.; Huffman, G. P.; Seehra, M. S. *IEEE Trans. Magn.* **2007**, *43*, 3091–3093.

(45) Koseuglu, Y. *J. Magn. Magn. Mater.* **2006**, *300*, e327–e330.

(46) Hsu, K. H.; Wu, J. H.; Huang, Y. Y.; Wang, L. Y.; Lee, H. Y.; Lin, J. G. *J. Appl. Phys.* **2005**, *97*, 114322.

(47) Seehra, M. S.; Srinivasan, G. *J. Appl. Phys.* **1982**, *53*, 8345–8347.

(48) Srinivasan, G.; Seehra, M. S. *Phys. Rev. B* **1983**, *28*, 1–7.

(49) López-Ortega, A. et al. *J. Am. Chem. Soc.* **2010**, *132*, 9398–9407.

(50) Kliava, J.; Edelman, I.; Ivanova, O.; Ivantsov, R.; Petrakovskaja, E.; Hennet, L.; Thiaudiere, D.; Saboungi, M. *J. Magn. Magn. Mater.* **2011**, *323*, 451–460.

(51) Park, J.; An, K.; Hwang, Y.; Park, J.-G.; Noh, H.-J.; Kim, J.-Y.; Park, J.-H.; Hwang, N.-M.; Hyeon, T. *Nat. Mater.* **2004**, *3*, 891–895.

(52) Salazar-Alvarez, G.; Sort, J.; Suriñach, S.; Baró, M. D.; Nogués, J. *J. Am. Chem. Soc.* **2007**, *129*, 9102–9108.

(53) Certain commercial equipment, instruments, and software, have been identified in this paper to foster understanding. Such identification does not imply recommendation or endorsement by the National Institute of Standards and Technology, nor does it imply that the materials or equipment identified are necessarily the best available for the purpose.

(54) Estradé, S.; Arbiol, J.; Peiró, F.; Abad, L.; Laukhin, V.; Balcells, L.; Martínez, B. *Appl. Phys. Lett.* **2007**, *91*, 252503.

(55) Estradé, S.; Arbiol, J.; Peiró, F.; Infante, I. C.; Sanchéz, F.; Fontcuberta, J.; de la Peña, F.; Walls, M.; Colliex, C. *Appl. Phys. Lett.* **2008**, *93*, 112505.

(56) Jr., T. C.; Newell, G. S.; Holton, W. C.; Slichter, C. P. *J. Chem. Phys.* **1960**, *32*, 668–673.

(57) Winkler, E.; Fainstein, A.; Etchegoin, P.; Fainstein, C. *Phys. Rev. B* **1999**, *59*, 1255–1262.

(58) Winkler, E.; Zysler, R. D.; Fiorani, D. *Phys. Rev. B* **2004**, *70*, 174406.

(59) Abragam, A., Bleaney, B., Eds. *Electron Paramagnetic Resonance of Transition Ions*; Dover Publications: New York, 1986.

(60) Morrish, A. H., Ed. *The Physical Principles of Magnetism*; IEEE: New York, 2001.

(61) de Biasi, E.; Ramos, C.; Zysler, R. *J. Magn. Magn. Mater.* **2003**, *262*, 235–241.

(62) Fainstein, A.; Winkler, E.; Butera, A.; Tallon, J. *Phys. Rev. B* **1999**, *60*, 12597–12600.

(63) Zhiwen, C.; Shuyuan, Z.; Shun, T.; Fanqing, L.; Jian, W.; Sizhao, J.; Yuheng, Z. *J. Cryst. Growth* **1997**, *180*, 280–283.

(64) Abbate, M.; Goedkoop, J. B.; Groot, M. F. D.; Grioni, M.; Fuggle, J. C.; Hofmann, S.; Petersen, H.; Sacchi, M. *Surf. Interface Anal.* **1992**, *18*, 65–69.

(65) Lee, H. J.; Kim, G.; Kim, D. H.; Kang, J.-S.; Zhang, C. L.; Cheong, S. W.; Shim, J. H.; Lee, S.; Lee, H.; Kim, J.-Y.; Kim, B. H.; Min, B. I. *J. Phys. Condens. Matter.* **2008**, *620*, 295203.

(66) Bayer, V.; Podloucky, R.; Franchini, C.; Allegretti, F.; Xu, B.; Parteder, G.; Ramsey, M. G.; Surnev, S.; Netzer, F. P. *Phys. Rev. B* **2007**, *76*, 165428.

(67) Chen, C. L. *Electronic and magnetic properties of transition metal ferrites and superlattice studied by X-ray Absorption spectroscopy.*; PhD Thesis: Tamkang University, 2005.

(68) Pellegrin, E. et al. *Phys. Status Solidi B* **1999**, *215*, 797–801.

(69) Pool, V.; Klem, M.; Jolley, C.; Arenholz, E. A.; Douglas, T.; Young, M.; Idzerda, Y. U. *J. Appl. Phys.* **2010**, *107*, 09B517.